

Constraining the cosmological baryon density with X-ray clusters

Claudio Gheller¹, Ornella Pantano² and Lauro Moscardini³

¹ *SISSA – International School for Advanced Studies, via Beirut 2–4, I–34013 Trieste, Italy*

² *Dipartimento di Fisica Galileo Galilei, Università di Padova, via Marzolo 8, I–35131 Padova, Italy*

³ *Dipartimento di Astronomia, Università di Padova, vicolo dell’Osservatorio 5, I–35122 Padova, Italy*

4 September 2018

ABSTRACT

We study the properties of X-ray galaxy clusters in four cold dark matter models with different baryon fraction Ω_{BM} ranging from 5 to 20 per cent. By using an original three-dimensional hydrodynamic code based on the piecewise parabolic method, we run simulations on a box with size $64 h^{-1}$ Mpc and we identify the clusters by selecting the peaks in the X-ray luminosity field. We analyse these mock catalogues by computing the mass function, the luminosity function, the temperature distribution and the luminosity-temperature relation. By comparing the predictions of the different models to a series of recent observational results, we find that only the models with low baryonic content agree with the data, while models with larger baryon fraction are well outside the $1\text{-}\sigma$ errorbars. In particular, the analysis of the luminosity functions, both bolometric and in the energy band $[0.5\text{--}2]$ keV, requires $\Omega_{BM} \lesssim 0.05$ when we fix the values $h = 0.5$ and $n = 0.8$ for the Hubble parameter and the primordial spectral index, respectively. Moreover we find that, independently of the cosmological scenario, all the considered quantities have a very little redshift evolution, particularly between $z = 0.5$ and $z = 0$.

Key words: Hydrodynamics – Large-scale structure of the Universe – X-ray: galaxies, general – Dark matter – Galaxies: clusters – Cosmology: theory

1 INTRODUCTION

Galaxy clusters are the most extended gravitationally bound systems of the Universe. In spite of their size, they are simple objects: their dynamics is governed essentially by the balance between gravitational and pressure forces, controlled by shock heating and adiabatic compression. Other processes, like radiative cooling in cluster cores or population III stars heating, may play a significant role only in some aspects of their history. For these reasons, the evolution and present day properties of clusters are very sensitive to the fundamental cosmological parameters and to the initial power spectrum. Therefore they provide an ideal tool to study the formation of the structures of the universe. Analytic techniques, as the Press-Schechter (1974) formalism, and numerical simulations, based on the Zel’dovich (1970) approximation or on more accurate N-body codes, have been extensively used to put strong constraints on the cosmological scenarios by comparing the model predictions to the observed abundances and clustering properties (see e.g. Borgani et al. 1997 and references therein).

It is well known that clusters have a large X-ray emission, essentially produced by thermal bremsstrahlung. The

quality of the observations in this band have been recently largely improved, providing new data which potentially can discriminate between different cosmological models. In order to compare these data to the numerical simulations we must include a reliable treatment of the hydrodynamic quantities, such as temperature, pressure and energy. For these reasons in the last years there has been a large effort of the cosmological community to develop new numerical codes which combine the standard N-body techniques, which solve the dynamics of the dark matter component, to hydrodynamic methods for properly following the evolution of the baryonic component (Hernquist & Katz 1989; Evrard 1990; Cen 1992; Steinmetz & Muller 1993; Ryu et al. 1993; Bryan et al. 1995; Gnedin 1995; Pen 1997; for a comparison of the different algorithms see Kang et al. 1994b). These codes have been applied for simulating in various cosmological models galaxy cluster properties and evolution and for calculating their masses, X-ray emission, mean temperature and the relations between these quantities, that is the fundamental information that is usually obtained from observational data (see e.g. Kang et al. 1994a; Bryan et al. 1994a,b; Navarro, Frenk & White 1995; Pen 1996; Cen 1997).

In this paper we apply a hydrodynamic code based on the coupling of the Piecewise Parabolic Method with the Particle-Mesh N-body code (Gheller, Pantano & Moscardini 1997) to study the large-scale distribution of the X-ray clusters in the framework of critical-density cold dark matter (CDM) models with a high baryon content (up to 20 per cent). This kind of model, allowed by the present uncertainties in the determination of the baryon density Ω_{BM} of the universe, when considered with a small tilt of the primordial spectral index ($n \approx 0.8$), has been suggested as possible solution of the problems of the standard (i.e. with $\Omega_{BM} \approx 0.05$ and $n = 1$) CDM model, namely the high small-scale power and the low first peak in the microwave anisotropy power spectrum (White et al. 1996). For a discussion about tilted models, see also Lucchin & Matarrese (1985); Vittorio, Matarrese & Lucchin (1988); Liddle & Lyth (1993).

The plan of the paper is as follows. In Section 2 we introduce the cosmological models that we consider. In Section 3 we present the numerical code and the method of cluster identification. The results are shown in Section 4. The main conclusions are drawn in Section 5.

2 COLD DARK MATTER MODELS WITH HIGH BARYON CONTENT

For a long period the CDM scenario has been the reference model for the interpretation of the observational data on the large scale of the universe. Its standard version assumes a flat universe with a density parameter $\Omega_0 = 1$, a Hubble constant $h = 0.5$ (in units of $100 \text{ km s}^{-1} \text{ Mpc}^{-1}$), a baryon contribution to the density Ω_{BM} fixed by the standard theory of big bang nucleosynthesis (BBN), and primordial fluctuations with Gaussian distribution and power spectrum $P(k) \propto k^n$, with $n = 1$. However, the normalization implied by the COBE detection of the microwave anisotropies (Smoot et al. 1992; see also Bennett et al. 1996) changed the situation, giving a spectrum with too much power on scales smaller than $10 h^{-1} \text{ Mpc}$. As a consequence, the CDM model is not able to reproduce either the clustering properties of galaxies and the distribution and abundances of clusters.

In order to solve the CDM problems, many alternatives have been proposed and discussed to reduce the short-scale power: tilted CDM models, i.e. with a primordial spectral index $n < 1$; mixed dark matter models, i.e. with the addition of a hot component corresponding to approximately 20 per cent of the total density; open CDM models, i.e. with $\Omega_0 < 1$; Lambda CDM models, i.e. with a non-vanishing cosmological constant fixed such as its contribution to the density is $\Omega_\Lambda = 1 - \Omega_0$; CDM models with a small Hubble constant, i.e. with $h < 0.5$. For a general review on the CDM model and its variants, see Liddle & Lyth (1993) and Coles (1996).

Very recently, it has been suggested (White et al. 1996) that also an increase of the baryon content Ω_{BM} can produce critical-density CDM models which fit the observational data in a reasonable way. In the past, the mean baryon density has been considered as a fixed quantity for most of cosmological models, in agreement with the predictions of the standard theory of BBN and the local estimates of light

elements abundances: $\Omega_{BM}h^2 = 0.0125 \pm 0.0025$, where the uncertainty is at 95 per cent confidence level.

The possibility of varying Ω_{BM} has been introduced because some recent observations have suggested that its estimate is much more uncertain than previously thought. In fact the first measurements of the deuterium abundance at high redshift yield very discrepant values. Small Ω_{BM} , in good agreement with the BBN predictions, are implied from different measurements of the neutral hydrogen column density in high-redshift clouds (Rugers & Hogan 1996a,b; Songaila, Wampler & Cowie 1997). On the contrary, the analyses performed by Tytler, Fan & Burles (1996) suggest $\Omega_{BM}h^2 = 0.024 \pm 0.002 \pm 0.002 \pm 0.001$, with the 1σ uncertainties being statistical, systematic and theoretical, respectively. These last results are also consistent with the lower limits obtained by Rauch et al. (1997) by comparing the observed flux decrement distribution function from a sample of seven high resolution QSO spectra to simulations of the Ly α forest. Similar conclusions have been reached also by Weinberg et al. (1997) by computing the amount of neutral hydrogen present in the high-redshift intergalactic medium necessary to produce the Ly α absorption in the QSO spectra. Finally, the determination of the baryonic fraction in clusters of galaxies (White et al. 1993; White & Fabian 1995; Elbaz, Arnaud & Böhringer 1995) leads, in a critical-density universe, to high values of Ω_{BM} . For example White & Fabian (1995) have calculated:

$$\frac{\Omega_{BM}}{\Omega_0} = 0.14_{-0.04}^{+0.08} \left(\frac{h}{0.5} \right)^{-3/2}, \quad (1)$$

again at the 95 per cent confidence.

By using a semi-analytical approach, White et al. (1996) carried out a general exploration of CDM models with high Ω_{BM} , allowing also the Hubble parameter h and the spectral index n to vary. The predictions of these scenarios have been compared with the observations of the clustering properties of galaxies, the cluster abundances, the statistics of the peculiar velocities, the formation of high-redshift objects (i.e. damped Ly α systems, Lyman break galaxies, quasars and clusters) and the cosmic microwave background anisotropies. Their final suggestion is that the models with Ω_{BM} in the range $[0.1-0.2]$, a Hubble parameter $h \approx 0.5$ and a small tilt in the primordial spectrum ($n \approx 0.8$), are in good agreement with all these data. A high baryonic fraction in fact helps “naturally” to suppress the short-scale power, as baryon collapse is stopped till decoupling, and, at the same time, amplifies the first peak of the CMB spectrum, compensating for the loss of height introduced by the tilt (needed to avoid too low values of h , excluded by the observational data). At the end of their analysis they conclude that these models can represent at the moment a viable alternative in the framework of critical-density CDM models.

In this paper we consider models where the universe is spatially flat, i.e. $\Omega_0 = \Omega_{DM} + \Omega_{BM} = 1$. Here Ω_{DM} is the density parameter of the (cold) dark matter component. We assume a vanishing cosmological constant ($\Omega_\Lambda = 0$). The initial spectrum of perturbations is defined as $P(k) \propto k^n T^2(k)$, where $T(k)$ is the CDM transfer function. We use the expression obtained by Bardeen et al. (1986):

$$T(q) = \frac{\ln(1 + 2.34q)}{2.34q} \times [1 + 3.89q +$$

Table 1. The parameters of the cosmological models. Column 2: the density parameter Ω_0 ; Column 3: the baryon density Ω_{BM} ; Column 4: the primordial spectral index n ; Column 5: the Hubble parameter h ; Column 6: the shape parameter Γ ; Column 7: the spectrum normalization σ_8 .

Model	Ω_0	Ω_{BM}	n	h	Γ	σ_8
BM05	1.0	0.05	0.8	0.5	0.44	0.77
BM10	1.0	0.10	0.8	0.5	0.41	0.72
BM15	1.0	0.15	0.8	0.5	0.39	0.66
BM20	1.0	0.20	0.8	0.5	0.36	0.61

$$(16.1q)^2 + (5.46q)^3 + (6.71q)^4]^{-1/4}, \quad (2)$$

where $q = k/h\Gamma$. The shape parameter Γ takes into account the dependence on the Hubble parameter h , on the total density Ω_0 and on the baryon density Ω_{BM} (Sugiyama 1995):

$$\Gamma = \Omega_0 h \exp(-\Omega_{BM} - \sqrt{h/0.5} \Omega_{BM}/\Omega_0). \quad (3)$$

As suggested by White et al. (1996), we have fixed $h = 0.5$ and $n = 0.8$, allowing the baryon content to vary. We consider four different values for Ω_{BM} : the usual value determined by the standard theory of BBN ($\Omega_{BM} = 0.05$); a baryon abundance consistent with the low deuterium measurements and with the more recent BBN calculations ($\Omega_{BM} = 0.1$); a value close to the estimate resulting from the cluster baryon fraction in the case of critical-density universe ($\Omega_{BM} = 0.15$); a more extreme case representing the upper limit of the range of observed cluster baryon fraction ($\Omega_{BM} = 0.2$). In the following we will label these four models as BM05, BM10, BM15 and BM20, respectively. The normalization of the spectrum, usually parametrized by σ_8 , the matter rms fluctuation in a top-hat sphere of radius $8 h^{-1}$ Mpc, is defined by the four-year COBE data (Bunn & White 1997). The cosmological parameters used for the different models are summarized in Table 1. Since the power at small scales (i.e. on large k) increases when Ω_{BM} decreases, we can expect a faster evolution in the models with low baryon content, with a larger production of big mass overdensities.

3 NUMERICAL METHOD

3.1 The code

The simulations have been evolved by using the numerical code presented in Gheller et al. (1997; see also Gheller, Moscardini & Pantano 1996), where we give a complete description of the method and we show the results of various numerical tests. Here we only summarize the main characteristics of the code.

The hydrodynamical part has been developed by using the Eulerian version of the Piecewise Parabolic Method (PPM; Colella & Woodward 1984) which ensures at least second-order (up to the fourth-order, in the case of smooth flows and small timesteps) accuracy in space and second-order accuracy in time. The high accuracy of this method allows minimization of errors due to the finite size of the cells of the grid and leads to a spatial resolution close to the nominal one (i.e. one grid). In a cosmological framework,

the basic PPM technique has been modified to include the gravitational interaction and the expansion of the universe. Particular care has been devoted to the calculation of the gas internal energy and a double formulation of the energy equation has been used in order to avoid large errors in the computation of thermodynamical quantities when the kinetic energy is very large compared to the internal one.

The hydrodynamical part has been coupled to a Particle Mesh (PM) N-body code (Hockney & Eastwood 1981) that describes the evolution of the dark component. The standard PM code has been modified in order to allow non-constant timesteps equal to those used in the integration of the hydrodynamical equations. This is obtained by replacing the standard second-order leapfrog method by a second-order two-step Lax-Wendroff scheme. Densities and forces are computed by using the cloud-in-cell interpolation scheme. The coupling is obtained by calculating, by the usual FFT procedure, the gravitational field due to both components.

In the simulations presented in this paper we neglected the atomic processes for radiative cooling since the cooling time of the hot gas produced in clusters is longer than a Hubble time. Moreover the only considered heating processes are the adiabatic compression and the entropy generation at shock fronts.

For each cosmological model we run one simulation with the initial conditions given by the same random sequence. The initial redshift, fixed in such a way that the maximum initial density fluctuation is less than unity, is approximately $z \approx 20$ for all models. The box-size has been fixed to $64 h^{-1}$ Mpc and the number of computational cells is 128^3 . Consequently the nominal spatial resolution, which our numerical tests have shown to be very close to the effective one (Gheller et al. 1997), is $0.5 h^{-1}$ Mpc. In the analysis of the results we have to be careful to properly evaluate the spurious effects that the limited box-size and the finite grid resolution can produce on the results. In fact the grid resolution prevents us from following the behaviour of matter inside a cell element. This can lead to underestimation of quantities like density and temperature, with a direct influence on the evolutionary history of the X-ray clusters. On the other hand, the limited size of the box has the effect of suppressing the large-scale power, reducing the possibility of forming very bright X-ray clusters with luminosity larger than 10^{45} erg s^{-1} . This kind of object is also likely to be partially missed in our simulations because it is rare: observational data (e.g. Henry & Arnaud 1991; Ebeling et al. 1997) show that in a box of $64 h^{-1}$ Mpc one expects to find at most one such object.

3.2 Cluster Identification

The first step of the data analysis consists of the identification of the X-ray clusters. We first calculate the emissivity due to thermal bremsstrahlung in a fully ionized plasma ($X = 0.76$, $Y = 0.24$) with temperature T (Rybicki & Lightman 1979; see also Evrard 1990):

$$\epsilon_\nu = 6.83 \times 10^{-38} Z^2 n_e n_i T^{-1/2} \times \bar{g}(h\nu/kT) e^{-h\nu/kT} \text{erg s}^{-1} \text{cm}^{-3} \text{Hz}^{-1}, \quad (4)$$

where $\bar{g}(h\nu/kT)e^{-h\nu/kT}$ is an average Gaunt factor, Z is the charge number, n_i and n_e are the ion and the electron density, respectively.

The bolometric emissivity, using a unit Gaunt factor, is defined as:

$$\begin{aligned}\epsilon_{bol} &= \int_0^\infty d\nu \epsilon_\nu \\ &= 1.42 \times 10^{-27} Z^2 n_i n_e T^{1/2} \text{erg s}^{-1} \text{cm}^{-3}.\end{aligned}\quad (5)$$

Then the energy radiated within a given energy band $E_1 - E_2$ can be expressed as

$$\epsilon_{band} = f_{band}(T) \epsilon_{bol}, \quad (6)$$

where

$$f_{band}(T) = \int_{E_1/kT}^{E_2/kT} d\eta \bar{g}(\eta) e^{-\eta}. \quad (7)$$

The band limited X-ray emission L_x from a given volume is computed integrating the previous expression over the relevant volume. Using the discretization of the simulation, the X-ray luminosity is

$$L_x = 1.25 \times 10^{-27} m_p^{-2} \sum_i \rho_{BMi}^2 T_i^{1/2} f_{band}(T_i) \text{erg s}^{-1}, \quad (8)$$

where the sum runs over cells within the volume, ρ_{BM} is the baryon density and m_p is the proton mass. Since we are interested only in X-ray emitting regions, it is safe to assume that the gas is completely ionized. We also set the Gaunt factor $\bar{g} = 1.2$: this gives an accuracy of ~ 20 per cent for the results.

At this point, in order to identify the clusters, we select the cells with $L_x \geq 10^{40} \text{erg s}^{-1}$ which are also local maxima in the X-luminosity field (i.e. their X-luminosity is greater than that of the 26 neighboring cells). These identify the cluster centres. A cluster is defined as the sum of the centre plus the 26 surrounding cells. In this way the total volume of a cluster equals the volume of a sphere of comoving radius $0.93 h^{-1} \text{Mpc}$, as appropriate for present observed X-ray clusters. In order to avoid double counting of the cells, the distance between cores is checked: if two cores are closer than $2 h^{-1} \text{Mpc}$ the fainter cluster is rejected from the catalogue. Finally, the cluster luminosity and the mass are calculated as the sum of the luminosity and density of each of its cells, respectively, while the temperature is defined as the average over the whole cluster volume.

4 RESULTS

4.1 Global properties

In Figure 1, we show a snapshot of the results in a slice of $64 \times 64 \times 0.5 h^{-3} \text{Mpc}^3$ at $z = 0$ for each of the four models. The baryonic matter density field ρ_{BM} , the dark matter density field ρ_{DM} , the gas temperature T and the X-ray emission L_x are presented in Figures 1a, 1b, 1c and 1d, respectively. Since the initial spectrum of fluctuations of all simulations has been generated by using the same random number sequence, the positions of the final structures are quite similar and the densities of each component scale approximatively according to their mean cosmic values. Matter

concentrates on filamentary structures and clusters form at the intersection of several filaments.

In the low- Ω_{BM} models, because of the larger power on small scales in the initial spectrum and the lower background pressure, shocks form earlier and are stronger than in the high- Ω_{BM} models. In the latter case, on the other hand, we can observe a stronger X-ray emission due to the higher baryon content of these models.

A close-up at four different redshifts of the most luminous X-ray cluster found in the BM05 simulation is presented in Figure 2. The slice is $20 \times 20 \times 0.5 h^{-3} \text{Mpc}^3$. It is evident the ongoing process of merging and the final virialized state characterized by an extended central isothermal region at high temperature. The cluster tends to a spherical geometry and deviations from sphericity are due to the cluster memory of its merging history (see e.g. Tormen 1997). These satellites, however, being faint X-ray sources, may not be observed in a X-ray map. Similar comments can be repeated for the other models (not shown here).

Dark matter structures appear typically less concentrate than the baryonic counterpart both in clusters and in filaments. In Table 2 we present the rms of the DM and BM density fields (σ_{DM} and σ_{BM} respectively) computed on the cell-size scale ($0.5 h^{-1} \text{Mpc}$) and the mean temperature $\langle T \rangle$ (in Kelvin degrees) at redshifts $z = 1$ and $z = 0$. The density contrasts of the two components are normalized to the corresponding mean cosmological values. A detailed analysis of the time evolution of the rms shows that at very high redshifts, due to absence of pressure forces, DM collapses faster than the baryonic counterpart. However, in all of our models, starting from about $z \sim 3$, baryons tend to concentrate more than the dark component. The absence of dissipative phenomena produces a spreading of DM around the minima of the gravitational potential, while BM, which tends to thermalize, concentrates there. As time goes by, also dark particles fall toward the centre of the potential well and at the final time the rms of the two components is quite similar (see Table 2).

Comparing the different models, we observe that both σ_{BM} and σ_{DM} decrease with the increasing of the baryon fraction both at $z = 1$ and $z = 0$. This behaviour is mainly related to the characteristics of the initial spectrum in the different models. Furthermore structures virialize earlier in low- Ω_{BM} models and shocks are stronger and the final temperatures higher than in the high- Ω_{BM} models, because of the lower pressure and higher densities present initially in these models. Between $z = 1$ and $z = 0$ there is a slightly faster evolution of structures in the case of a high baryon content and this is probably favoured by the lower temperatures produced in this case.

4.2 X-ray cluster mass

Clusters in our simulations are identified through their X-ray emission and their characteristic properties, like the total mass, the total luminosity and the mean temperature, are computed by integrating or averaging over a fixed number of cells, as explained in Section 3.2. The values of these quantities could then be affected by the choice of the number of cells used for the calculation. Several tests have shown that our procedure provides good estimates for the temperature and the luminosity of the cluster. In fact the temperature is

Table 2. The global properties of the model simulations. The rms of the dark matter, σ_{DM} , the rms of the baryonic matter, σ_{BM} , and the mean temperature $\langle T \rangle$ (in Kelvin degrees), computed on the cell scale, are shown at redshift $z = 1$ (Columns 2, 3 and 4) and at $z = 0$ (Columns 5, 6 and 7).

Models	σ_{DM}	σ_{BM}	$\langle T \rangle$ K	σ_{DM}	σ_{BM}	$\langle T \rangle$ K
			$z = 1$			$z = 0$
BM05	3.27	3.40	4.86×10^5	7.31	7.34	1.04×10^6
BM10	2.80	3.14	3.86×10^5	6.97	7.00	9.24×10^5
BM15	2.44	2.73	2.97×10^5	6.05	6.27	7.68×10^5
BM20	1.94	2.20	2.20×10^5	5.33	5.45	6.35×10^5

almost uniform over regions greater than those over which we do our averaging. Moreover the luminosity is proportional to the square of the baryonic density and then its value depends essentially on the cells with highest density which represents the centre of the cluster and which are consequently always included in our integration. The inclusion or missing of some low-density cells does not affect sensibly our estimates for the temperature and the luminosity, but could affect the calculation of the cluster total mass. In summing over a fixed number of cells we tend to overestimate the mass of objects which are not as extended as our reference volume (27 cells) and which are also usually characterized by density lower than the mean cluster values. The opposite is true for large clusters, although in this case we have verified that, for our choice of the reference volume, the error introduced in the estimation of the mass is less severe and it is at most a factor two. Therefore we have restricted our analysis to clusters with mass greater than $10^{14} M_{\odot}$ (for $h = 0.5$). This lower limit has been fixed in order to avoid the inclusion of too low-mass objects which can be affected by a large error in the mass estimate and whose properties differ considerably from those of a typical galaxy cluster (e.g., their mean density is much lower than that determined from observations). Furthermore their spatial distribution could be affected by the X-luminosity selection criterion used to build our cluster catalogue.

In Figure 3 we present, for the four models, the number N_M of clusters with mass greater than $10^{14} M_{\odot}$ found in the whole simulation box at various redshifts. The number of clusters decreases with increasing Ω_{BM} at any redshift. This is a consequence of the amount of power on small scales, which decreases as we increase the baryonic fraction. In the high- Ω_{BM} cases the collapse of massive objects occurs later and, then, if we select clusters by their mass, the models with high baryonic fraction presents less clusters than low- Ω_{BM} models. The behaviour of the mass function depends on the distribution of the total (dark plus baryonic) density and then it is not the preferred quantity for discriminating between our models. Other quantities, like the X-ray luminosity, that depends directly on the BM density, appear to be a more useful quantity for the problem studied in the present paper.

Notice that the estimated N_M roughly agrees with the observational data for all the models. This is an expected result, because of the spectra normalizations. In fact it is known that the present abundance of galaxy clusters re-

Table 3. The X-ray emissivity (in units of $10^{40} \text{ ergs s}^{-1} h^3 \text{ Mpc}^{-3}$) for the gas (j_{gas}) and for the clusters (j_{cl}) at various redshifts for the different models.

	BM05		BM10		BM15		BM20	
	j_{gas}	j_{cl}	j_{gas}	j_{cl}	j_{gas}	j_{cl}	j_{gas}	j_{cl}
$z = 1$	0.17	0.12	0.49	0.39	0.66	0.49	0.73	0.55
$z = 0.7$	0.21	0.16	0.54	0.43	0.79	0.62	0.98	0.79
$z = 0.5$	0.20	0.15	0.63	0.46	0.88	0.73	1.53	0.86
$z = 0.2$	0.19	0.14	0.51	0.39	0.87	0.73	1.29	1.12
$z = 0$	0.16	0.13	0.59	0.50	0.96	0.81	1.05	0.85

quires, in the framework of the critical-density models and almost independently of the shape of the primordial spectrum, a normalization $\sigma_8 \approx 0.6$, with a quite large uncertainty (e.g. White, Efstathiou & Frenk 1993; Viana & Liddle 1996; Eke, Cole & Frenk 1996).

4.3 X-ray cluster luminosity

In Figure 4 we present the number of clusters with luminosity greater than $L_x = 10^{42}$ and $10^{43} \text{ erg s}^{-1}$ (N_{42} and N_{43} , respectively). This luminosity-based selection criterion leads to results opposite to those obtained by selecting clusters by their masses. In fact at any epoch the number of clusters increases with increasing Ω_{BM} . Furthermore the evolution of N_{42} and N_{43} with redshift is not monotonic: the number of clusters tends to grow until a turn-around redshift after which it starts to decrease. This behaviour is common to all the models and for both the adopted minimum luminosity. The only exception is N_{43} in the case of BM05, which grows continuously with time, but, because of the small number, this might be not statistically significant. The turn-around is due to the balance between the mechanisms driving the cluster evolution, and it is an indication of the epoch when the merging processes of different structures start to dominate over the gravitational collapse of each single object. In fact the merging leads to larger but smoother structures. Since the X-ray emission is proportional to the square of the baryonic density, lower luminosities are expected. The effect of the merging processes is also shown by the simultaneous decrease in the number of fainter clusters (not reported in the figure). The turn-around redshift becomes lower with increasing the baryon fraction ranging from $z = 0.7$ for BM05 to $z = 0.2 - 0.5$ for BM20. This is due to the delayed evolution of the structures in high- Ω_{BM} models.

This behaviour is confirmed by the X-ray emissivity per unit comoving volume due to both the gas in its entirety, j_{gas} , and the clusters, j_{cl} (see Table 3). For each model the two quantities evolve in a parallel way, indicating that clusters emit roughly a constant large fraction of the total X-ray radiation. Similar results have been obtained, for the standard CDM model, also by Kang et al. (1994a) and Bryan et al. (1994a).

The fundamental differences between the cluster abundances in mass (N_M) and in X-ray luminosity (N_{42} and N_{43}) must be kept in mind when the results are compared to the observations. In Figure 5 we present the luminosity function

for the four models computed at five different redshifts, integrated over the whole range of frequencies. Very bright clusters with luminosity greater than 10^{45} erg s $^{-1}$ are missing in our simulations. The lack of such clusters can be related to two different effects. Firstly, the size of our computational box limits the amount of large-scale power which we can follow in the simulation, and consequently the maximum temperature that can be produced. Secondly, the grid resolution is likely to underestimate the highest density peaks where brightest clusters are expected to form.

The luminosity functions have been fitted by using a two-parameter function:

$$n(L)dL = n_0 L^{-\alpha} dL, \quad (9)$$

where $n(L)dL$ is the comoving density of clusters with luminosity between L and $L+dL$, n_0 is in units of $10^{-6} h^3 \text{Mpc}^{-3}$ and L is in units of 10^{44} erg s $^{-1}$. The results of the fits are presented in Table 4. Notice that for our data a two-parameter fit is more appropriate than the usual Schechter function, as in our results the expected bend at high L is not present, for the reasons given above.

The values of the slope α cannot discriminate between the four models, as the differences are in general within the $1-\sigma$ errorbars. The parameter α shows for all the models a slight negative evolution with redshift from $z = 0.5$ to $z = 0$; this behaviour is thought to be the effect of the ongoing processes of gravitational collapse, that produces more concentrated and bright structures, and merging, that leads to the formation of larger and more massive objects at the expenses of the smaller ones. For the normalizations n_0 , which is the comoving number density of objects with luminosity equal to 10^{44} erg s $^{-1}$, we can make considerations similar to those previously made for N_{42} and N_{43} .

The hatched region in the figure shows the observational data (with $1-\sigma$ errorbars) of Ebeling et al. (1997) which refer to the ROSAT Brightest Cluster sample containing 199 objects with redshift $z \leq 0.3$. The observational curves have been fitted by the authors by using a three-parameter function:

$$n(L) = A \exp(-L/L^*) L^{-\alpha}, \quad (10)$$

where A is in units of $10^{-7} \text{Mpc}^{-3} (10^{44} \text{erg s}^{-1})^{\alpha-1}$ and L^* is in units of $10^{44} \text{erg s}^{-1}$. The values of the fitting parameters are $A = 6.41_{-0.61}^{+0.70}$, $L^* = 37.2_{-3.8}^{+16.4}$ and $\alpha = 1.84_{-0.04}^{+0.09}$.

We can compare these data with the results of the simulations at low redshifts. The models with high baryonic content (BM15 and BM20) have a luminosity function which is significantly too high with respect to the observations. On the contrary the BM05 model and (much more marginally) BM10 are in better agreement with the data.

Similar conclusion can be obtained if we consider the luminosities in the energy band [0.5–2] keV. The fitting parameters for our simulations are reported in Table 5, while the comparison with two different observational datasets is shown in Figure 6. The vertically hatched region refers again to the Ebeling et al. (1997) sample, whose luminosity function has been fitted by a three-parameter relation (10) with $A = 3.32_{-0.33}^{+0.36}$, $L^* = 5.70_{-0.93}^{+1.29}$ and $\alpha = 1.85_{-0.09}^{+0.09}$. The horizontally hatched region shows instead the results obtained by De Grandi (1996) using a complete flux-limited ROSAT sample selected from the ESOKP redshift survey: in this case the fitting parameters are $A = 4.51$, $L^* = 2.63_{-0.58}^{+0.87}$ and

$\alpha = 1.32_{-0.23}^{+0.21}$. These two determinations of the luminosity functions are in good agreement for luminosities larger than $\approx 2 \times 10^{43}$ erg s $^{-1}$, while for smaller L_x the De Grandi (1996) results are approximately a factor 3 smaller than the Ebeling et al. (1997) ones, increasing the discrepancies between the observations and the model predictions of the models with high Ω_{BM} .

In this energy band there is a further luminosity function determined by Burns et al. (1996), always by using images from the ROSAT all-sky survey. Because of the large errorbars, it completely overlaps both the previous results and for clarity we prefer do not show it in Figure 6. However, since in this dataset also nearby poor clusters have been considered, this result allows to extend the previous considerations also to smaller X-ray luminosities (less than 10^{42} erg s $^{-1}$), not included in the other datasets.

4.4 X-ray cluster temperatures

In Figure 7 we show the redshift evolution of the distribution of the cluster mean temperature for the four models. The temperatures have been calculated as emission-weighted averages because this is the quantity which is also usually estimated from the observations. The absence of clusters with temperatures above 4 keV is mainly related to the limited size of the box and their rareness. These model predictions can be compared with the observations. In the figure the hatched region refers to the temperature distribution obtained by Henry & Arnaud (1991) from a set of local ($z \approx 0$) clusters:

$$n(T) = (1.8_{-0.5}^{+0.8} \times 10^{-3} h^3 \text{Mpc}^{-3} \text{keV}^{-1}) T^{-4.7 \pm 0.5}, \quad (11)$$

where the uncertainties are $1-\sigma$ errorbars and T is expressed in keV.

All the models are in quite good agreement with observations in the overlapping range. Temperature is in fact less sensitive than luminosity to the details of the density distribution and it is related to the maximum wavelength λ of non-linear waves. In fact the post-shock temperature is of the order of $T \propto (H\lambda)^2$, where H is the Hubble constant. Low- Ω_{BM} models have a higher normalization of the primordial spectrum and longer wavelengths can reach the non-linear regime at the final time producing higher values of the temperature. This phenomenon is likely to be strengthened by the different mean background pressure of the various realizations, which is lower in low- Ω_{BM} models. Both effects could explain the higher number of objects with temperature larger than about 1 keV found with decreasing Ω_{BM} .

We have also analysed the redshift evolution of the temperature distributions in our simulations. We found that between $z = 1$ and $z = 0$ such distributions are almost constant for BM05 and BM10 models, with a slow increase in the number of high-temperature objects. In these models, by $z \sim 1$ the regions heated up by shocks at almost a uniform temperature are larger than the integration volume of our cluster identification method. In general, from that moment, the temperature of these regions increases because of adiabatic compression and merging processes and this explains the rise in the number of high-temperature clusters towards $z = 0$. The models BM15 and BM20, instead, evolve rapidly between $z = 1$ and $z = 0.5$, showing in particular a strong

Table 4. The parameters of the fits of the X-ray cluster bolometric luminosity function $n(L) = n_0 L^{-\alpha}$ at various redshifts for the different models.

	BM05		BM10		BM15		BM20	
	α	n_0	α	n_0	α	n_0	α	n_0
$z = 1$	1.82 ± 0.09	6.73 ± 0.06	1.72 ± 0.08	18.95 ± 0.23	1.59 ± 0.07	31.66 ± 0.38	1.74 ± 0.06	18.56 ± 0.15
$z = 0.7$	1.73 ± 0.15	9.72 ± 0.18	1.72 ± 0.09	21.55 ± 0.30	1.71 ± 0.05	26.60 ± 0.24	1.73 ± 0.07	28.44 ± 0.33
$z = 0.5$	1.74 ± 0.20	8.42 ± 0.20	1.75 ± 0.16	19.46 ± 0.47	1.76 ± 0.09	25.66 ± 0.36	1.69 ± 0.08	33.20 ± 0.46
$z = 0.2$	1.61 ± 0.07	12.50 ± 0.12	1.68 ± 0.04	20.97 ± 0.12	1.69 ± 0.05	29.12 ± 0.24	1.69 ± 0.11	35.59 ± 0.72
$z = 0$	1.41 ± 0.11	23.11 ± 0.48	1.67 ± 0.11	18.68 ± 0.31	1.62 ± 0.05	31.69 ± 0.25	1.66 ± 0.03	33.95 ± 0.15

Table 5. The parameters of the fits of the X-ray cluster luminosity function $n(L) = n_0 L^{-\alpha}$ computed in the [0.5–2] keV band at various redshifts for the different models.

	BM05		BM10		BM15		BM20	
	α	n_0	α	n_0	α	n_0	α	n_0
$z = 1$	1.47 ± 0.11	11.73 ± 0.17	1.43 ± 0.07	19.26 ± 0.24	1.39 ± 0.10	19.19 ± 0.31	1.40 ± 0.11	10.17 ± 0.13
$z = 0.7$	1.58 ± 0.40	8.40 ± 0.49	1.55 ± 0.11	15.73 ± 0.26	1.58 ± 0.11	12.90 ± 0.20	1.45 ± 0.12	18.25 ± 0.32
$z = 0.5$	1.81 ± 0.16	5.52 ± 0.04	1.58 ± 0.12	15.09 ± 0.28	1.52 ± 0.07	22.51 ± 0.30	1.57 ± 0.10	28.56 ± 0.48
$z = 0.2$	1.44 ± 0.11	13.71 ± 0.27	1.55 ± 0.06	15.87 ± 0.17	1.67 ± 0.08	13.63 ± 0.15	1.55 ± 0.11	21.31 ± 0.52
$z = 0$	1.36 ± 0.17	18.05 ± 0.60	1.63 ± 0.17	11.75 ± 0.28	1.61 ± 0.06	11.75 ± 0.28	1.57 ± 0.09	19.28 ± 0.28

growth in the number density of objects with temperature greater than about 0.5 keV. This corresponds to the later formation and propagation of the shocks in these models. In fact after $z = 0.5$ the situation becomes similar to that of the low- Ω_{BM} models, and the temperature distributions show little further evolution.

4.5 Luminosity-Temperature relation

In Figure 8 we present the distribution of emission-weighted temperature of the clusters as a function of the X-ray bolometric luminosity at three different redshifts: $z = 1$ (crosses), $z = 0.5$ (open circles) and $z = 0$ (filled circles). For all the models there is a similar trend in the luminosity-temperature relation, even though the total number of objects grows with the baryon fraction. We observe that a given temperature corresponds to higher luminosities in high- Ω_{BM} models. This is related to the higher baryonic densities present in these cases.

The luminosity-temperature distributions have been fitted by using a power-law relation of the form $T = 10^b L_x^\eta$, where T is in keV and L_x is in units of $10^{40} \text{ erg s}^{-1}$. The results, reported in Table 6, show that for all the models there is a little evolution with time, especially between $z = 0.5$ and $z = 0$, where present-day observational data are available. In particular the parameter η is always inside the $1-\sigma$ errorbar range, even if the models with smaller baryonic content tend to have a steeper slope. The normalization b , instead, slightly decreases with increasing redshift and/or Ω_{BM} . This result is in qualitative agreement with the more recent observational analysis, which found no evolution of

the temperature-luminosity distribution, at least for $z < 0.5$ (Mushotzky & Scharf 1997).

Our results can be directly compared to the observational data. The hatched region in Figure 8 shows the L_x - T relation (always with $1-\sigma$ errorbars) obtained by Henry & Arnaud (1991) for clusters with luminosity larger than $10^{44} \text{ erg s}^{-1}$. Even if the statistics are poor, the most luminous clusters for all the models are in good agreement with these data. The dotted line, instead, shows the fit from the combined sample of David et al. (1993), which contains clusters with lower luminosities ($L_x > 10^{42} \text{ erg s}^{-1}$). In this case the dispersion of the data around the fit (not explicitly reported in the original paper) is of the same order of that showed for the Henry & Arnaud (1991) results. The models with high baryonic fraction, even if they reproduce well the slope of the relation, have a lower normalization: at the same luminosity, the temperature is at least a factor 3 smaller than for the observations. The agreement is better for BM05 and BM10 models which have a steeper (but still consistent) slope.

Notice that it is not possible to present a comparison with the relation obtained by Mushotzky & Scharf (1997) because it refers to clusters with luminosities higher than those reached in our simulations.

5 CONCLUSIONS

In this work we have studied the evolution and the properties of X-ray clusters of galaxies in four different critical-density CDM-like models, in which the baryon fraction has been varied from $\Omega_{BM} = 0.05$ to $\Omega_{BM} = 0.20$. Models with a baryonic content larger than the predictions of the standard nucleosynthesis have been firstly considered by White et al.

Table 6. The parameters of the fits of the Luminosity-Temperature relation $T = 10^b L_x^\eta$, computed at various redshifts for the different models.

	BM05		BM10		BM15		BM20	
	η	b	η	b	η	b	η	b
$z = 1$	0.41 ± 0.04	-1.22 ± 0.09	0.34 ± 0.03	-1.31 ± 0.07	0.30 ± 0.04	-1.38 ± 0.10	0.31 ± 0.04	-1.52 ± 0.11
$z = 0.7$	0.40 ± 0.03	-1.10 ± 0.07	0.33 ± 0.03	-1.20 ± 0.09	0.31 ± 0.04	-1.32 ± 0.09	0.30 ± 0.03	-1.42 ± 0.08
$z = 0.5$	0.42 ± 0.03	-1.06 ± 0.07	0.35 ± 0.03	-1.17 ± 0.09	0.33 ± 0.03	-1.28 ± 0.07	0.30 ± 0.03	-1.35 ± 0.07
$z = 0.2$	0.42 ± 0.02	-0.99 ± 0.06	0.36 ± 0.02	-1.11 ± 0.06	0.33 ± 0.02	-1.17 ± 0.06	0.31 ± 0.03	-1.25 ± 0.08
$z = 0$	0.40 ± 0.02	-0.90 ± 0.06	0.37 ± 0.02	-1.05 ± 0.05	0.35 ± 0.02	-1.14 ± 0.05	0.32 ± 0.02	-1.20 ± 0.06

(1996) who found that they are in good agreement with a large set of observational data when coupled with a small tilt in the primordial spectrum ($n \approx 0.8$). Our results have proved to be useful in order to discriminate between the various models and to decide which of these models, if any, is compatible with observations.

The mass function, the luminosity function, and the luminosity-temperature relation are the quantities that gave the most important hints on the properties of the models. The behaviour of these quantities is determined by the dynamical evolution of the clusters. This is driven from the balance of two phenomena: the gravitational collapse of single objects and the merging of different structures. In the early stages of the evolution, the first effect tends to dominate, and the X-ray emission grows rapidly. The collapse of the baryonic matter is stopped by the formation of the shock. This rises strongly the pressure of the matter that finally is able to contrast the gravitational infall. Then the smaller virialized objects start to merge together, forming larger structures characterized by smoother density fields and hence by lower X-ray emission.

The mass function presents the expected behaviour, with the cluster number density that, at $z = 0$ decreases with increasing baryon fraction. This is mainly due to the different amount of power on small scales in the initial spectra of the density fluctuations. This result is obtained by identifying clusters only by their mass, without considering their luminosity. On the other hand, when clusters are selected by their total X-ray luminosity, the opposite trend is found: high- Ω_{BM} models have the higher number density of X-ray clusters. This is essentially related to the presence of more baryons and so to the formation of higher baryonic density peaks that then leads to much higher X-luminosity, this quantity depending on the square of the baryonic density itself. The X-ray emission depends also on the cluster temperatures but these are roughly the same for all the models.

Another difference is shown by the time evolution: while the number of clusters with large mass is a growing function of time for all the models, the abundance of luminous X-ray clusters starts to decrease at a some redshift, which is dependent on the cosmological model, being lower for high- Ω_{BM} models.

We compare the predictions of the four different cosmological models to a series of observational results, mainly referring to local ($z \approx 0$) datasets. By analysing the luminosity function and (more marginally) the luminosity-temperature

relation we can conclude that the models with low baryonic content ($\Omega_{BM} \lesssim 0.05$) are in better agreement with the data, while models with 15 or 20 per cent are well outside the 1- σ errorbars. On the contrary the study of the cluster temperature distribution cannot distinguish between the various models. Our result is even more stringent if we observe that our resolution tends to underestimate the luminosities; consequently the differences of the high- Ω_{BM} models with observations would be even higher. Therefore the X-ray properties seem to exclude that the increase of the baryonic content can help to reconcile, in the framework of critical-density models, the cold dark matter scenario with the observations.

In order to investigate if the differences found in the results for the various cosmological models are due to the different power spectrum normalization (i.e. σ_8), we ran a second simulation for the BM15 model, but adopting in this case the same σ_8 value of the BM05 model which we found previously to be the model in better agreement with the X-ray cluster data. As expected, in this new simulation with a higher normalization (hereafter BM15_{hn}) the number N_M of clusters with mass greater than $10^{14} M_\odot$ is larger than in the BM15 model: we found $N_M = 28$ and 72 at $z = 0.5$ and $z = 0$, respectively. These results are comparable to those obtained for the BM05 model, confirming that the mass function depends mainly on the spectrum normalization. A similar comment can be done for the rms of the dark and baryonic matter and for the mean temperature computed on the cell scale. We also observe a larger formation of X-ray clusters in the BM15_{hn} model than in the BM15 model: at $z = 0$ we found $N_{42} = 136$ and $N_{43} = 38$. The resulting luminosity functions, both bolometric and in the energy band [0.5–2] keV, are slightly higher than those of the BM15 model, increasing the difference with the observational datasets. A stronger discrepancy with the data is also obtained when the luminosity-temperature relation is considered. All these results support the idea that an increase of the primordial baryonic fraction with respect to the standard values (approximately 5 per cent) produces X-ray clusters with properties in disagreement with the available data. Of course this is obtained by assuming a particular set of parameters, namely $n = 0.8$ and $h = 0.5$ and it would be interesting to know if the conclusion survives when these parameters are varied inside the range still allowing an acceptable fit to other data (see White et al. 1996).

Finally, another important feature which we found in our simulations is the very little redshift evolution of X-

ray cluster properties. In all of our models, the luminosity function, the temperature distribution and the luminosity-temperature relation for the simulated clusters are almost constant, particularly between $z = 0.5$ and $z = 0$, in good agreement with that which seems to emerge also from very recent observational data.

ACKNOWLEDGMENTS

We would like to thank A. Heavens, F. Lucchin, S. Matarrese and G. Tormen for a critical reading of the manuscript. We are grateful also to A. Cavaliere for useful discussions. Finally, the referee Andrew Liddle is acknowledged for valuable comments and criticisms which improved the presentation of the results. This work was partially supported by Italian MURST.

REFERENCES

Bardeen J.M., Bond J.R., Kaiser N., Szalay A.S., 1986, *ApJ*, 304, 15
 Bennett C.L., et al., 1996, *ApJ*, 464, L1
 Borgani S., Moscardini L., Plionis M., Górski K.M., Holtzman J., Klypin A., Primack J.R., Smith C.C., Stompor R., 1997, *NewA*, 1, 321
 Bryan G.L., Cen R., Norman M.L., Ostriker J.P., Stone J.M., 1994a, *ApJ*, 428, 405
 Bryan G.L., Klypin A., Loken C., Norman M.L., Burns J.O., 1994b, *ApJ*, 437, L5
 Bryan G.L., Norman M.L., Stone J.M., Cen R.Y., Ostriker J.P., 1995, *Comput. Phys. Comm.*, 89, 149
 Bunn E.F., White M., 1997, *ApJ*, 480, 6
 Burns J.O., Ledlow M.J., Loken C., Klypin A., Voges W., Bryan G.L., Norman M.L., White R.A., 1996, *ApJ*, 467, L49
 Cen R., 1992, *ApJS*, 78, 341
 Cen R., 1997, *ApJ*, 485, 39
 Colella P., Woodward P., 1984, *J. Comput. Phys.*, 54, 174
 Coles P., 1996, *Contemp. Phys.*, 37, 429
 David L.P., Slyz A., Jones C., Forman W., Vrtilek S.D., Arnaud K.A., 1993, *ApJ*, 412, 479
 De Grandi S., 1996, in *Proc. of Röntgenstrahlung from the Universe*, ed. Zimmermann H.U., Trümper J., Yorke H. (Munich: MPE), 577
 Ebeling H., Edge A.C., Fabian A.C., Allen S.W., Crawford C.S., Böhringer H., 1997, *ApJ*, 479, L101
 Eke V.R., Cole S., Frenk C.S., 1996, *MNRAS*, 282, 263
 Elbaz D., Arnaud M., Böhringer H., 1995, *A&A*, 393, 337
 Evrard A.E., 1990, *ApJ*, 363, 349
 Gheller C., Moscardini L., Pantano O., 1996, *MNRAS*, 283, 1184
 Gheller C., Pantano O., Moscardini L., 1997, *MNRAS*, in press, astro-ph/9701170
 Gnedin N.Y., 1995, *ApJS*, 97, 231
 Henry J.P., Arnaud K.A., 1991, *ApJ*, 372, 410
 Hernquist L., Katz N.S., 1989, *ApJS*, 64, 715
 Hockney R.W., Eastwood J.W., 1981, *Computer Simulations Using Particles*. McGraw-Hill, New York, NY
 Kang H., Cen R., Ostriker J.P., Ryu D., 1994a, *ApJ*, 428, 1
 Kang H., Ostriker J.P., Cen R., Ryu D., Hernquist L., Evrard A.E., Bryan G.L., Norman M.L., 1994b, *ApJ*, 430, 83
 Liddle A.R., Lyth D.H., 1993, *Phys. Rep.*, 231, 1
 Lucchin F., Matarrese S., 1985, *Phys. Rev.*, D32, 1316
 Mushotzky R.F., Scharf C.A., 1997, *ApJ*, 482, L13
 Navarro J.F., Frenk C.S., White S.D.M., 1995, *MNRAS*, 275, 720
 Pen U.-L., 1996, preprint, astro-ph/9610147

Pen U.-L., 1997, preprint, astro-ph/9704258
 Press W.H., Schechter P., 1974, *ApJ*, 187, 452
 Rauch M., et al., 1997, *ApJ*, in press, astro-ph/9612245
 Rugers M., Hogan C.J., 1996a, *ApJ*, 459, L1
 Rugers M., Hogan C.J., 1996b, *AJ*, 111, 2135
 Rybicki G.B., Lightman A.P., 1979, *Radiative Processes in Astrophysics*. Wiley & Sons, New York, NY
 Ryu D., Ostriker J.P., Kang H., Cen R., 1993, *ApJ*, 414, 1
 Smoot G.F., et al., 1992, *ApJ*, 396, L1
 Songaila A., Wampler E.J., Cowie L.L., 1997, *Nat*, 385, 137
 Steinmetz M., Muller E., 1993, *A&A*, 268, 391
 Sugiyama N., 1995, *ApJS*, 100, 281
 Tormen G., 1997, *MNRAS*, 290, 411
 Tytler D., Fan X.-M., Burles S., 1996, *Nat*, 381, 207
 Viana P.T.P., Liddle A.R., 1996, *MNRAS*, 281, 323
 Vittorio N., Matarrese S., Lucchin F., 1988, *ApJ*, 328, 69
 Weinberg D.H., Miralda-Escudé J., Hernquist L., Katz N., 1997, *ApJ*, in press, astro-ph/9701012
 White D.A., Fabian A.C., 1995, *MNRAS*, 273, 72
 White M., Viana P.T.P., Liddle A.R., Scott D., 1996, *MNRAS*, 283, 107
 White S.D.M., Navarro J.F., Evrard A.E., Frenk C.S., 1993, *Nat*, 366, 429
 White S.D.M., Efstathiou G., Frenk C.S., 1993, *MNRAS*, 262, 1023
 Zel'dovich Ya.B., 1970, *A&A*, 5, 84

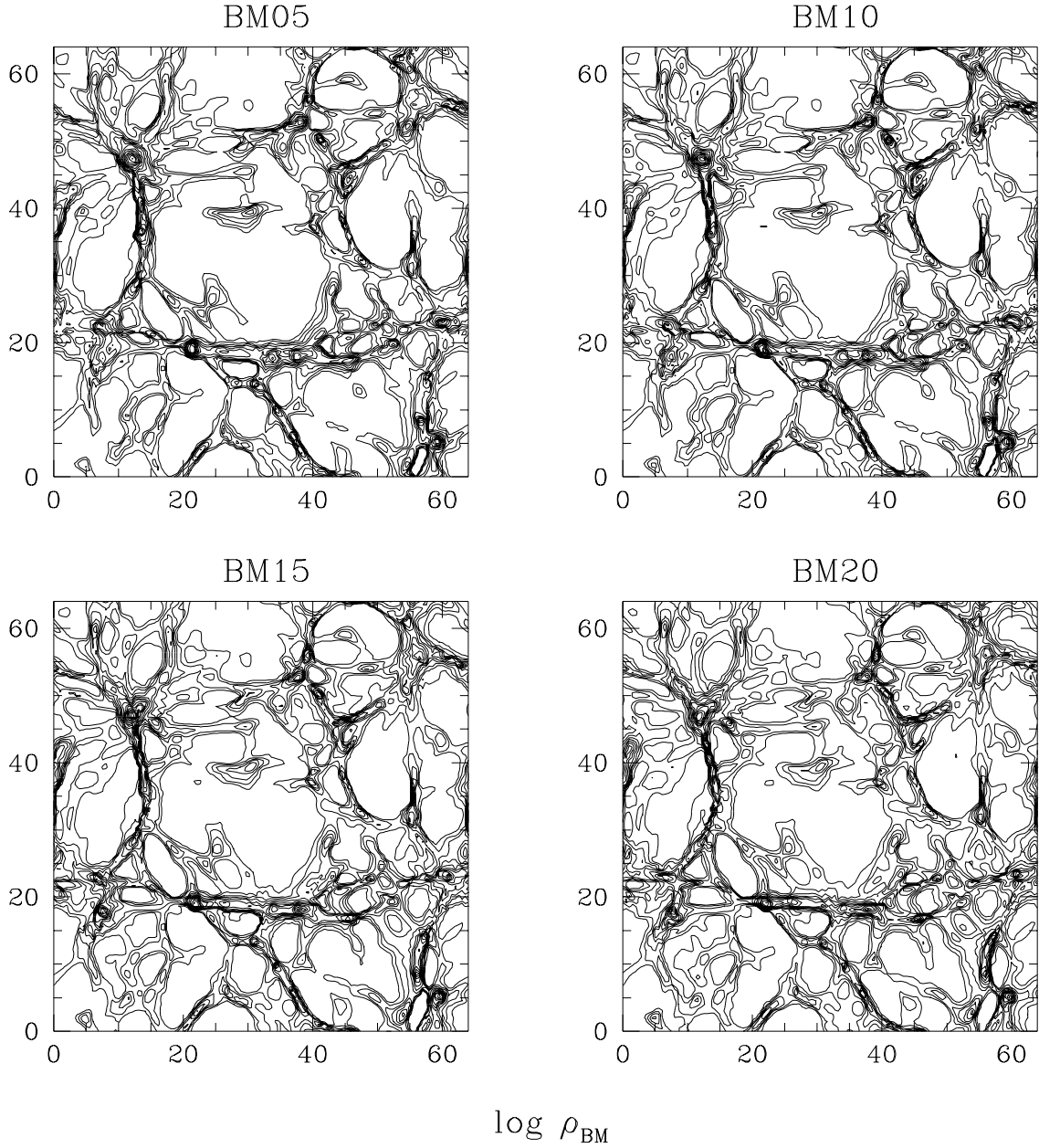


Figure 1. a. The contour plots for the baryonic density ϱ_{BM} in a slice of $64 \times 64 \times 0.5 h^{-3} \text{ Mpc}^3$ at $z = 0$ for the four different models: BM05 (top left), BM10 (top right), BM15 (bottom left), BM20 (bottom right). The baryonic density is normalized to its mean density and the contour levels correspond to $10^{(i-3)/4}$, where $i = 1, 2, \dots, 15$

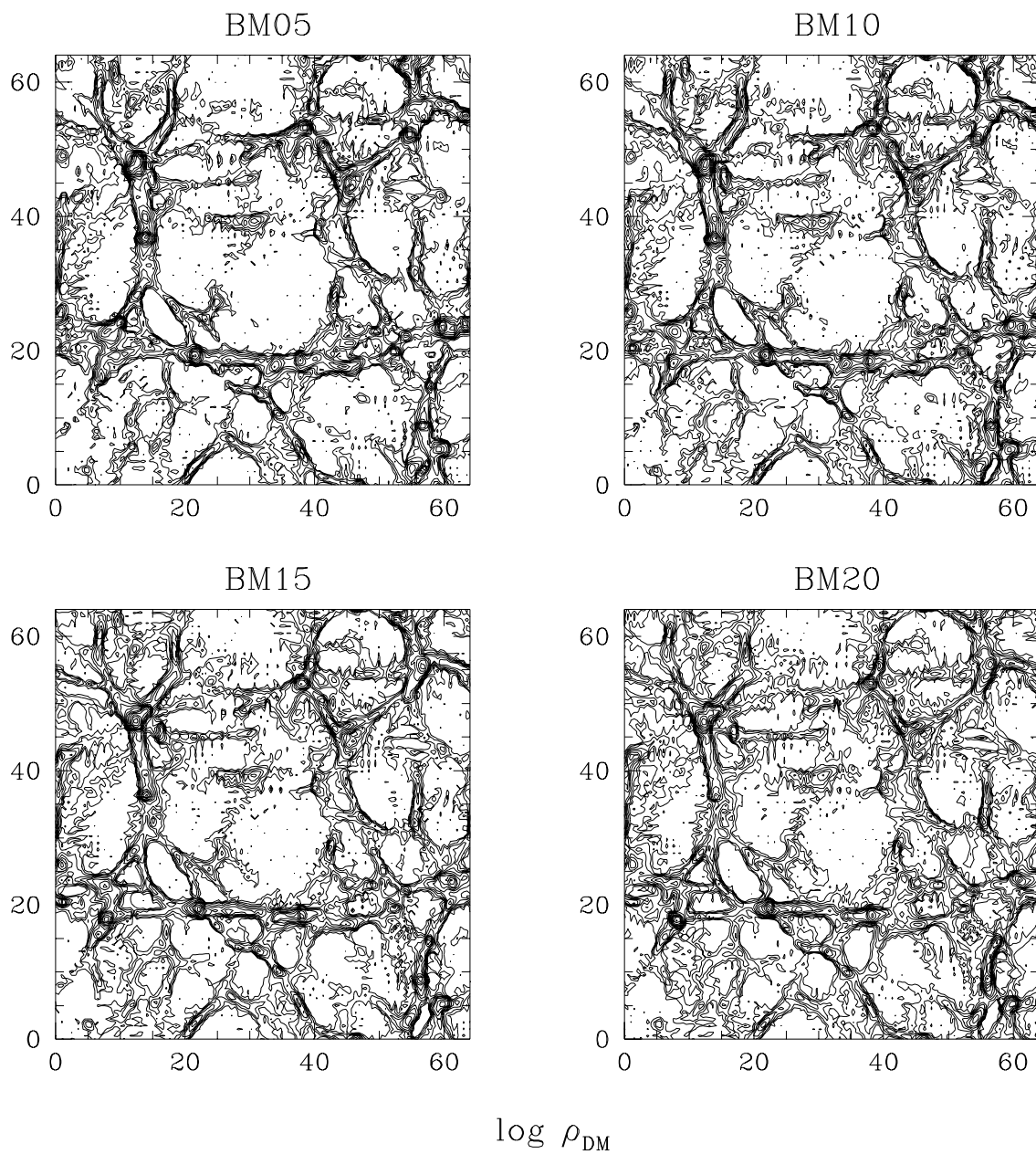


Figure 2. *

b. The same as Figure 1a but for the dark matter density ρ_{DM} which is normalized to its mean density. The contour levels correspond to $10^{(i-3)/4}$, where $i = 1, 2, \dots, 14$

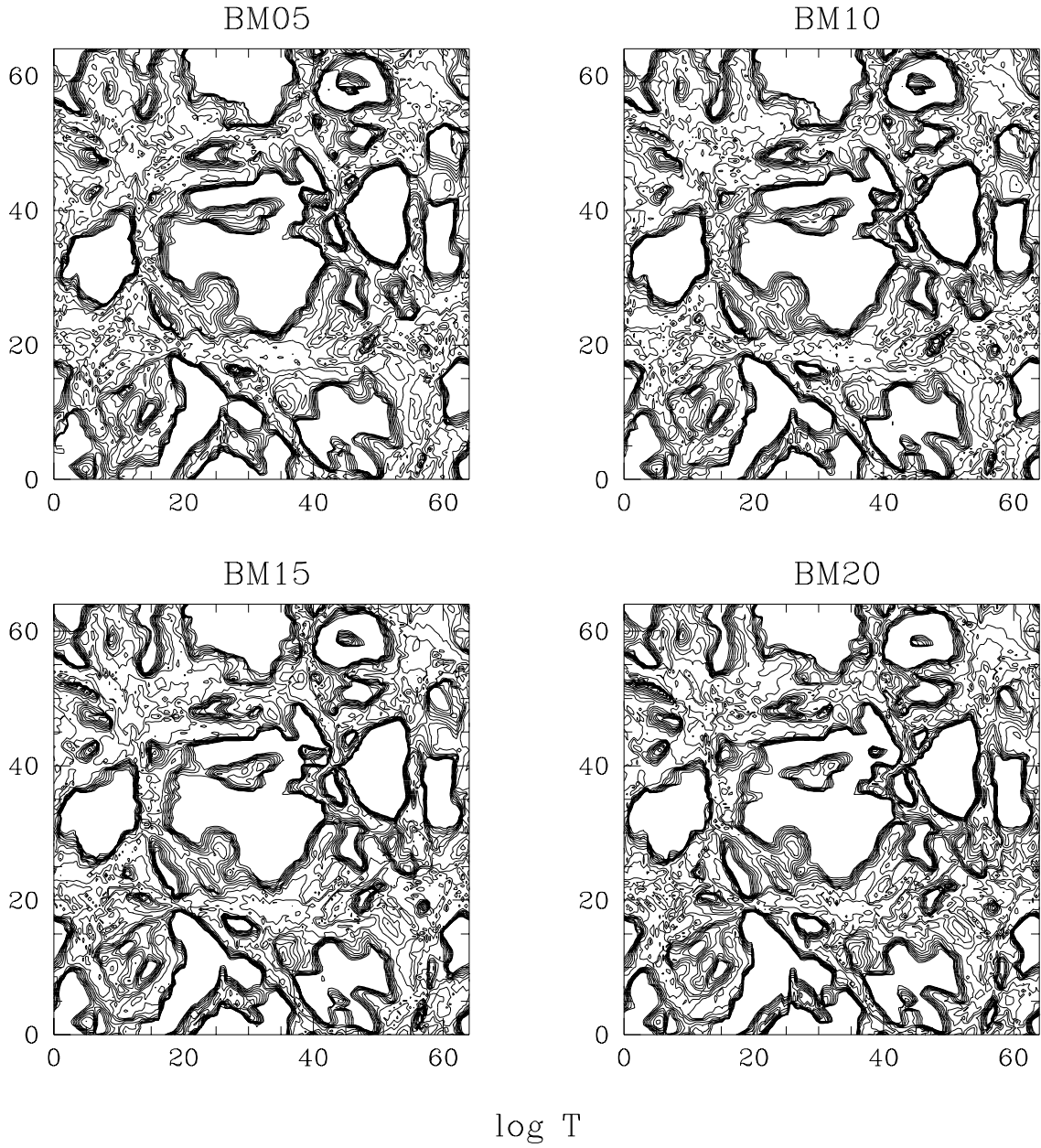


Figure 3. *

c. The same as Figure 1a but for the temperature T which is in units of Kelvin degrees. The contour levels correspond to $10^{2i/3}$, where $i = 1, 2, \dots, 12$

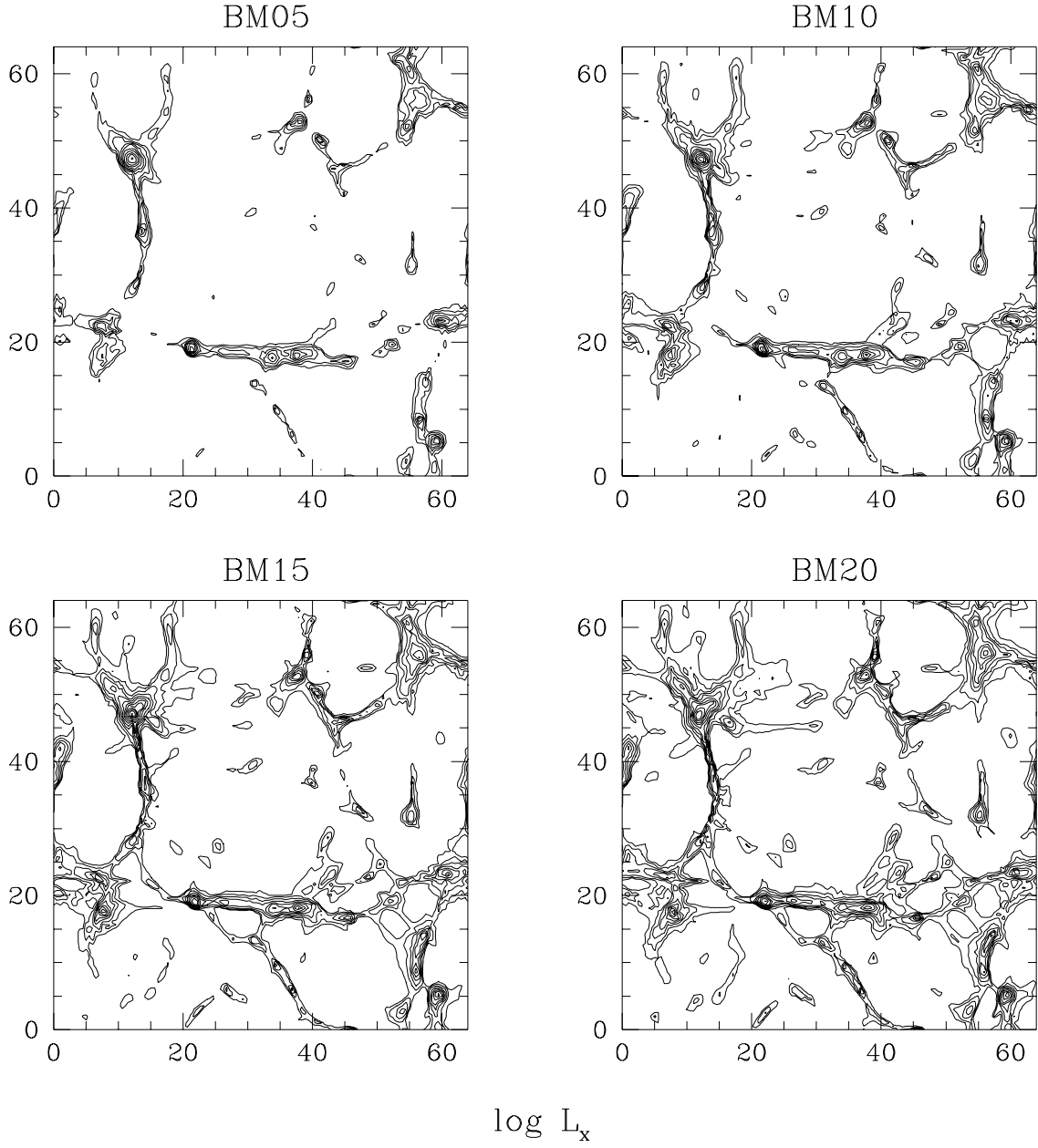
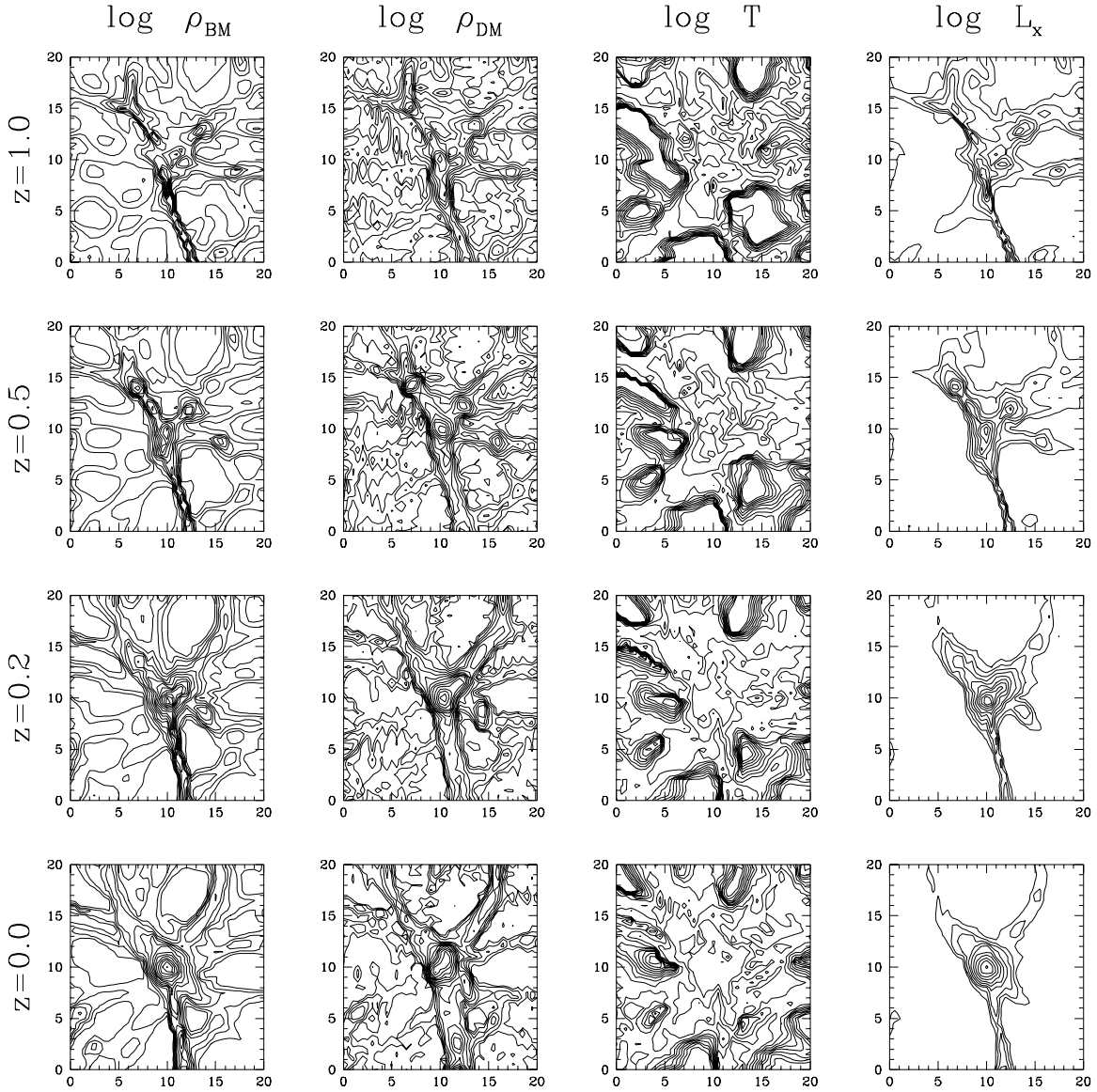


Figure 4. *

d. The same as Figure 1a but for the X-ray luminosity L_x which is in units of 10^{36} erg s^{-1} . The contour levels correspond to $10^{2i/3}$, where $i = 1, 2, \dots, 11$



BM05

Figure 5. The contour plots for the baryonic density ρ_{BM} (first column), the dark matter density ρ_{DM} (second column), the temperature T (third column) and the X-ray luminosity L_x (last column) in a slice of $20 \times 20 \times 0.5 h^{-3} \text{ Mpc}^3$ around the most luminous cluster in the BM05 simulation. The different rows show the redshift evolution: $z = 1$, $z = 0.5$, $z = 0.2$ and $z = 0$ from the top to the bottom. The density of each component is normalized to its mean density while the temperature and the luminosity are in units of Kelvin degrees and $10^{36} \text{ erg s}^{-1}$, respectively. The density contour levels correspond to $10^{(i-3)/4}$ while the temperature and the luminosity levels are $10^{2i/3}$, where $i = 1, 2, \dots$

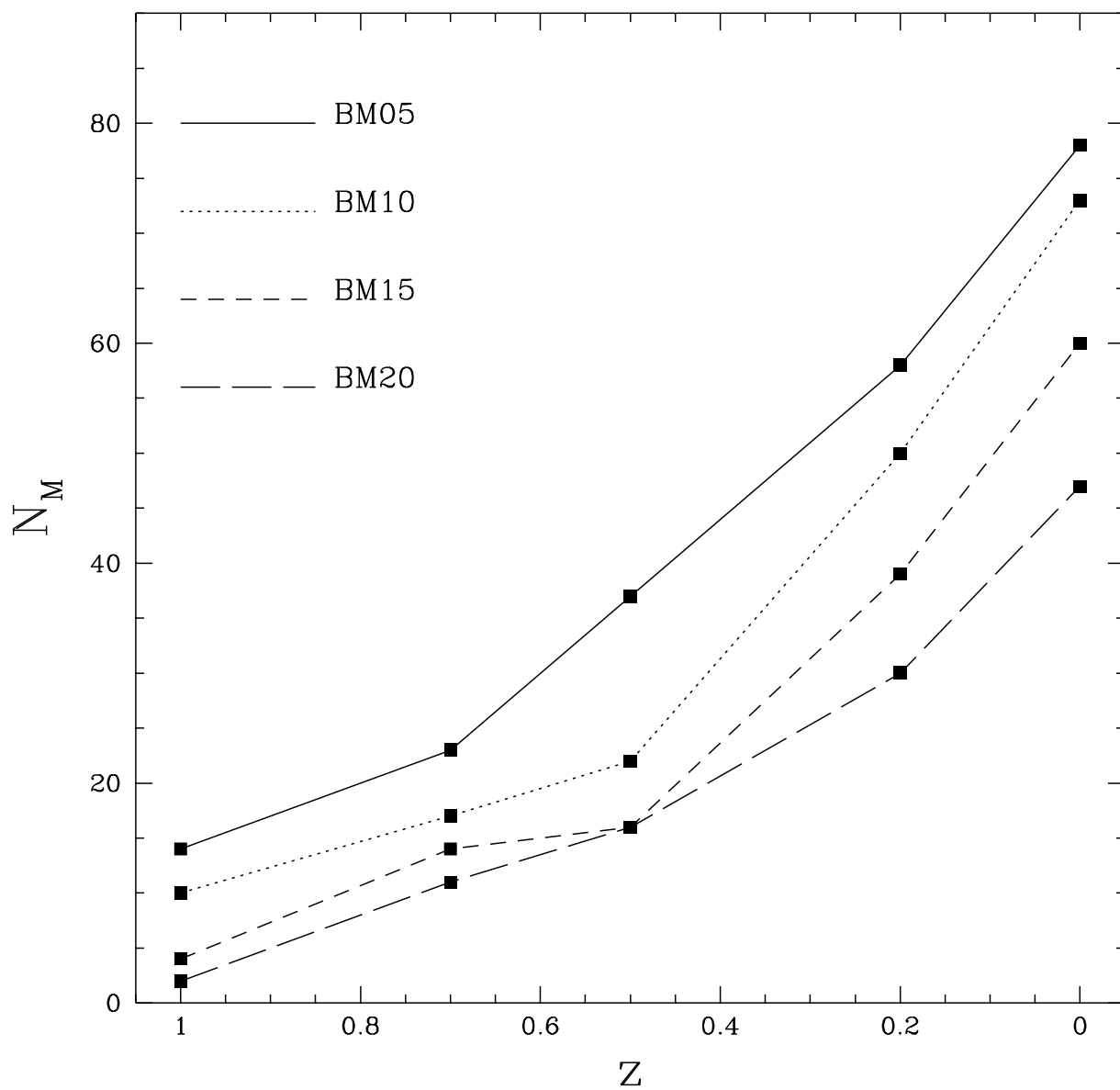


Figure 6. The number of clusters N_M with mass $\geq 10^{14} M_\odot$ as a function of the redshift z for the different models: BM05 (solid line), BM10 (dotted line), BM15 (short-dashed line) and BM20 (long-dashed line).

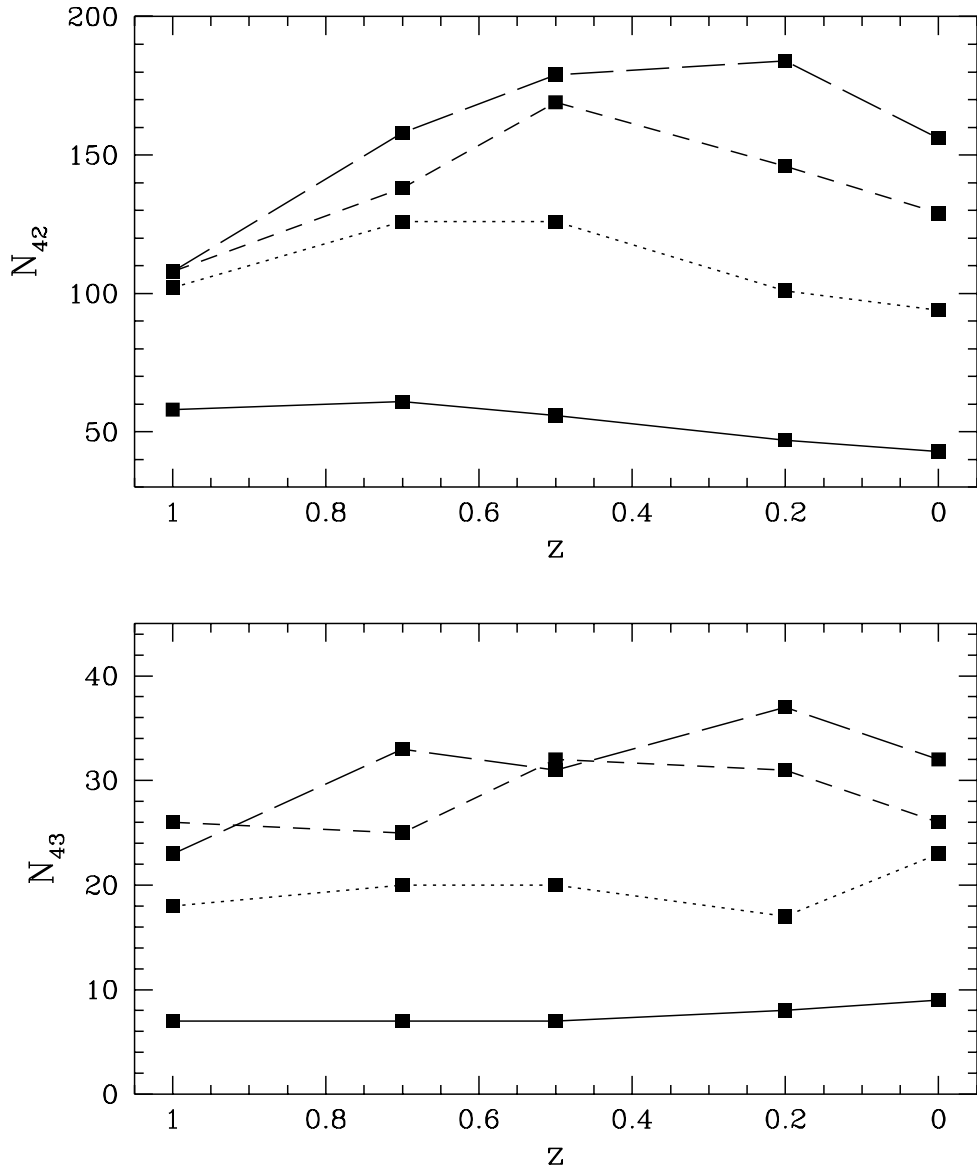


Figure 7. The number of clusters with luminosity $L_x \geq 10^{42}$ (N_{42} , upper panel) and $L_x \geq 10^{43}$ erg s $^{-1}$ (N_{43} , bottom panel) as a function of the redshift z for the different models: BM05 (solid line), BM10 (dotted line), BM15 (short-dashed line) and BM20 (long-dashed line).

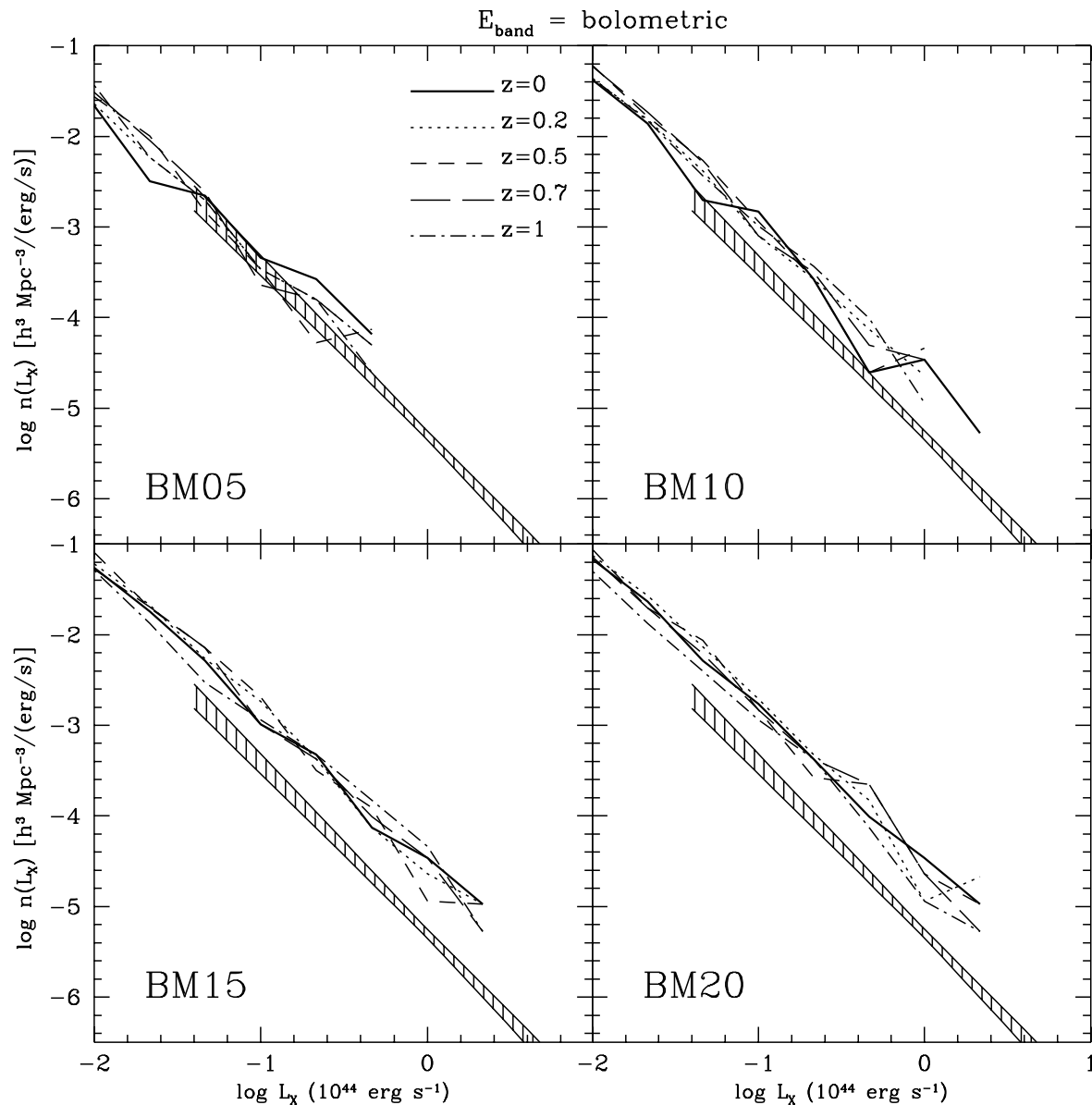


Figure 8. The cluster bolometric luminosity function for the different models: BM05 (top left), BM10 (top right), BM15 (bottom left) and BM20 (bottom right). The different curves refer to various redshift: $z = 0$ (solid line), $z = 0.2$ (dotted line), $z = 0.5$ (short-dashed line), $z = 0.7$ (long-dashed line), $z = 1$ (dotted-dashed line). The hatched region shows the observational results (with $1-\sigma$ errorbars) obtained by Ebeling et al. (1997).

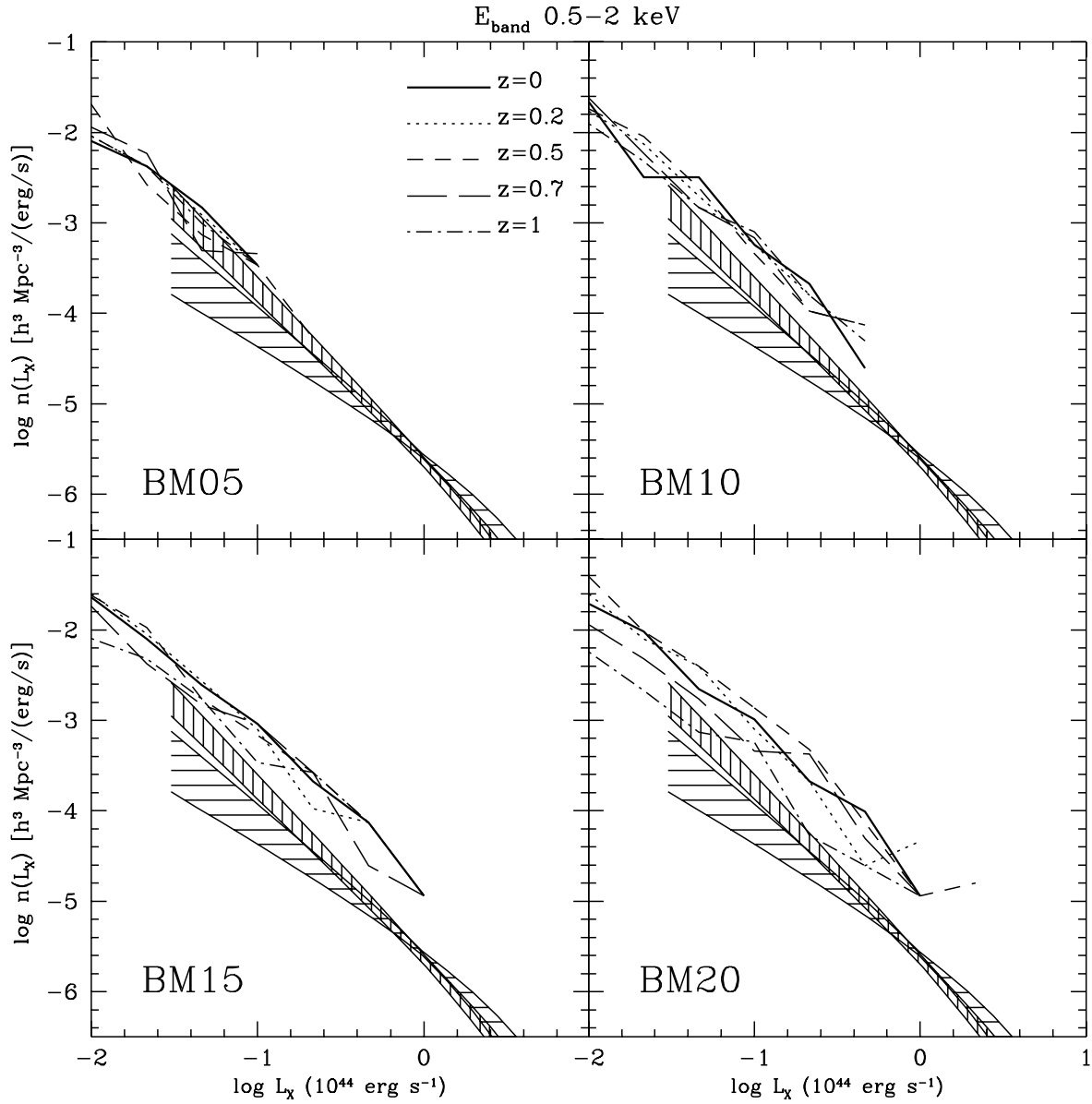


Figure 9. The same as Figure 5 but in the [0.5–2] keV energy band. The vertically hatched region shows the observational results (with $1-\sigma$ errorbars) obtained by Ebeling et al. (1997), while the horizontally hatched one refers to the De Grandi (1996) results.

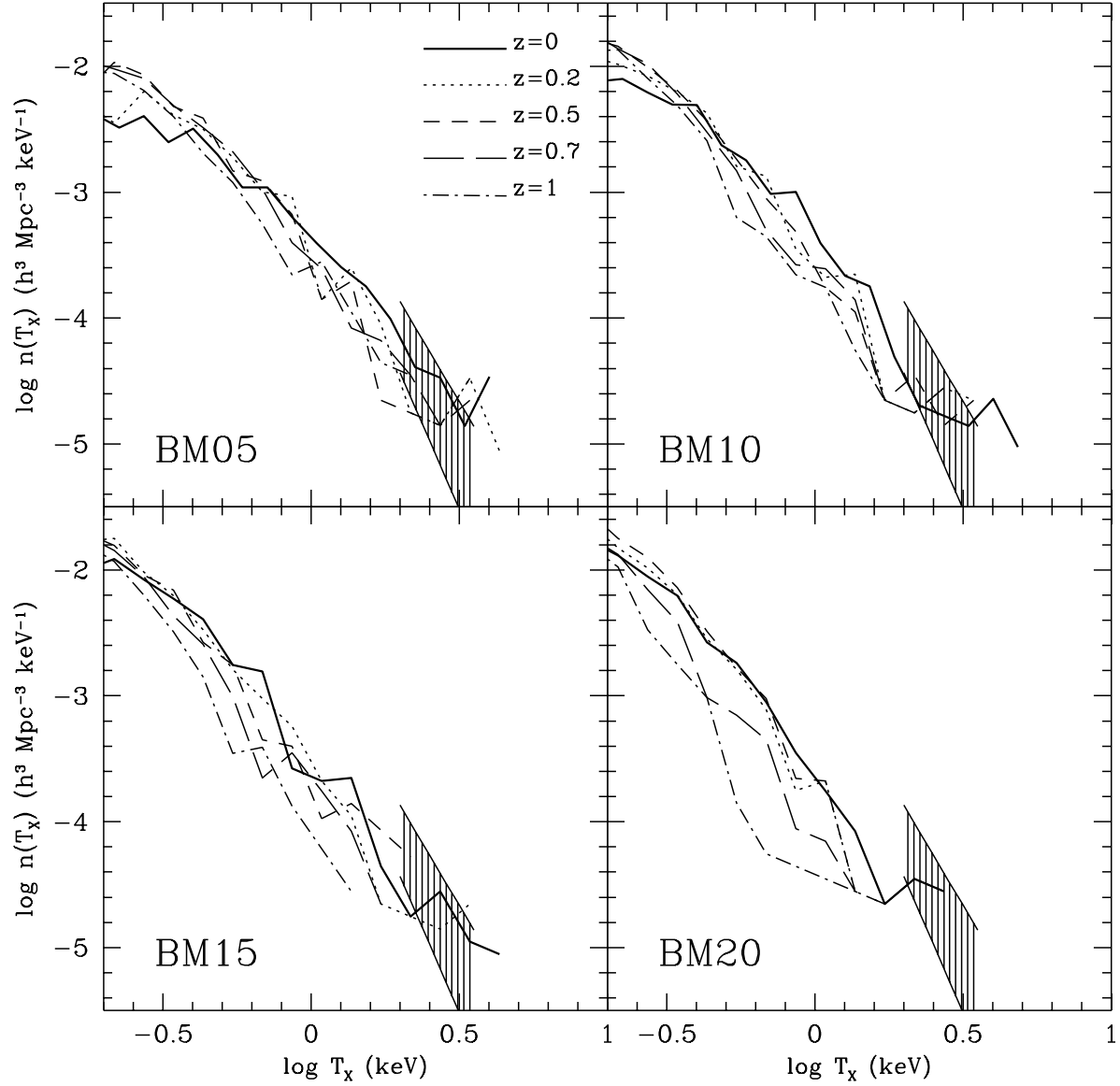


Figure 10. The cluster temperature function for the different models: BM05 (top left), BM10 (top right), BM15 (bottom left) and BM20 (bottom right). The different curves refer to various redshift: $z = 0$ (solid line), $z = 0.2$ (dotted line), $z = 0.5$ (short-dashed line), $z = 0.7$ (long-dashed line), $z = 1$ (dotted-dashed line). The hatched region shows the observational results (with $1\text{-}\sigma$ errorbars) obtained by Henry & Arnaud (1991).

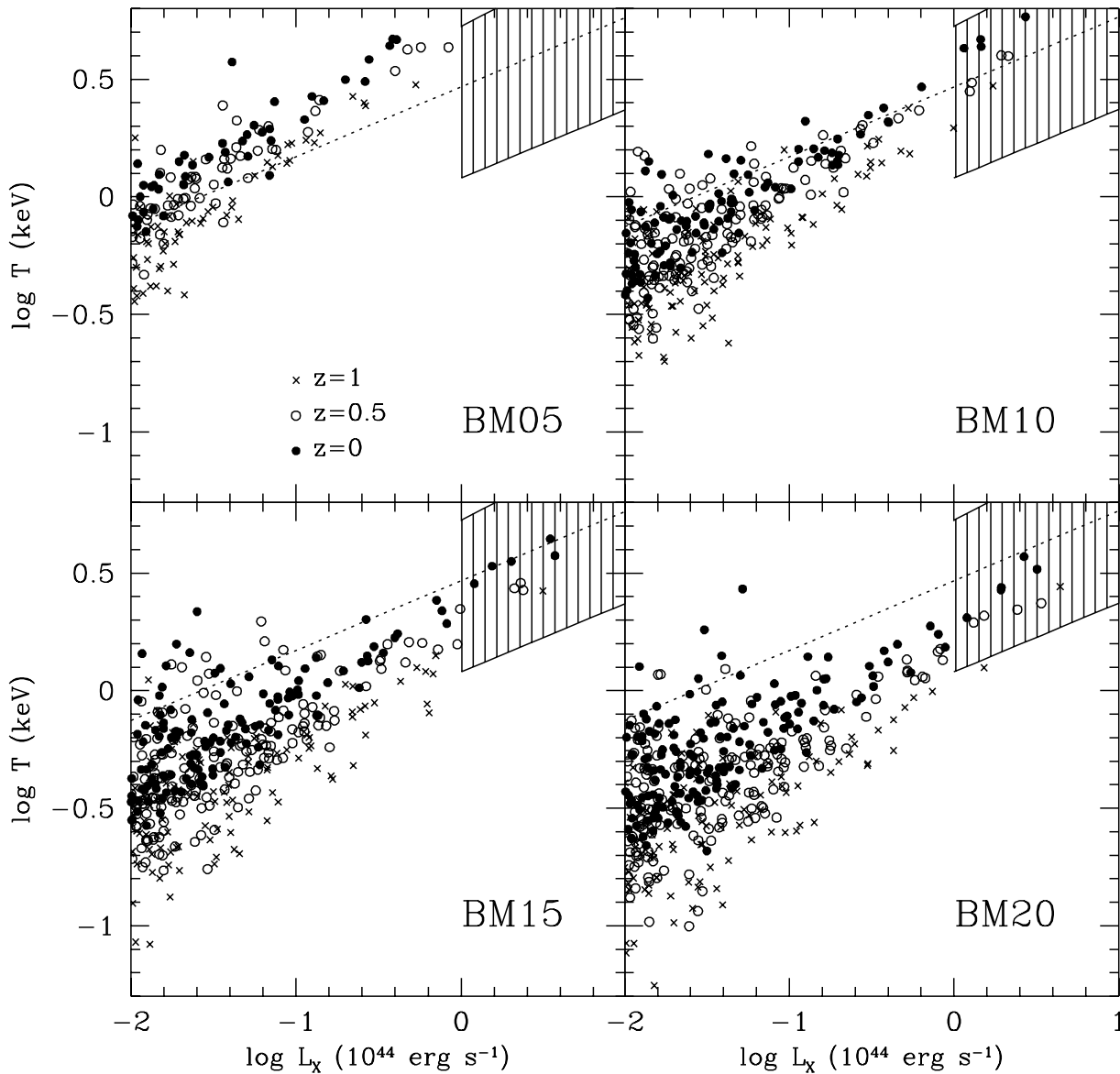


Figure 11. Scatter plots of the bolometric X-ray luminosity L_x and the emission-weighted temperature T of the clusters for the different models: BM05 (top left), BM10 (top right), BM15 (bottom left) and BM20 (bottom right). Different redshifts are displayed by different symbols: $z = 1$ (crosses), $z = 0.5$ (open circles) and $z = 0$ (filled circles). The hatched region shows the observational results (with $1-\sigma$ errorbars) obtained by Henry & Arnaud (1991); the dotted line refers to the fit obtained from the combined sample of David et al. (1993). In this last case the errorbars are not explicitly reported, but they are of the same order of magnitude of the previous ones.